Rock Mechanics and Rock Engineering (2023) 56:6983–7001
https://doi.org/10.1007/s00603-023-03418-9

ORIGINAL PAPER

Performance Evaluation of AE Sensors Installed Like Hydrophones in Adaptive Monitoring Networks During a Decametre-Scale Hydraulic Stimulation Experiment

Carolin M. Boese[1] · Grzegorz Kwiatek[1] · Katrin Plenkers[2] · Thomas Fischer[2] · Georg Dresen[1]

Received: 12 April 2022 / Accepted: 19 May 2023 / Published online: 11 July 2023

Abstract

In the framework of the STIMTEC and STIMTEC-X hydraulic stimulation experiments at the Reiche Zeche mine, Freiberg (Germany), we installed acoustic emission (AE) sensors for the recording of picoseismicity both conventionally using pneumatic coupling and experimentally like a hydrophone, i.e. the sensors were placed in the borehole without a further coupling system or cementing. We investigate performance measures of the hydrophone-like acoustic emission (HAE) sensors such as frequency bandwidth, sensitivity, first motion polarity, coupling and placement quality to assess the sensor's applicability in adaptive monitoring networks. HAE sensors can be paired with hydraulic equipment, especially with the double packer probe used for stimulation at the decametre scale because the monitored frequency content differs from injection-related noise. This offers a unique opportunity to improve the network geometry and consequently the quality of a seismic catalogue. We analyse the sensor characteristics using active ultrasonic transmission measurements from boreholes with different orientations in the rock volume, noise measurements preceding active centre punch hits in the access galleries and passive recordings of induced acoustic emission events. HAE sensors placed in water-filled boreholes show good sensitivity performance even without optimal coupling to the crystalline rock for recording distances up to 17 m. The HAE sensors record the wavefield adequately for first-arrival identification, polarity picking and amplitude characteristics but are less suitable for detecting S-waves. Due to the borehole geometry HAE sensors record waves with incidence angles from the side, resulting in opposite polarity compared to side-view AE sensors as observed in the field and lab. We discuss the advantages of adaptive monitoring networks with HAE sensors being optimally placed for each stimulation interval configuration anew to improve seismic event detection and quality of event hypocentre locations during hydraulic stimulations. We show that we are able to significantly reduce the azimuthal gap, halve the location uncertainties and improve the network coverage for the purpose of focal mechanism estimations.

Highlights

- An adaptive network comprising acoustic emission (AE) sensors installed both conventionally by pneumatic coupling and like hydrophones was used to significantly improve detection and localisation quality.
- Hydrophone-like AE-sensors placed in water-filled boreholes show good sensitivity performance for recording distances up to 17 m in crystalline rocks.
- Hydrophone-like AE-sensors can be combined with hydraulic equipment because the monitored frequency content differs from injection-related noises.

✉ Carolin M. Boese
cboese@gfz-potsdam.de

[1] Helmholtz Centre Potsdam, GFZ German Research Centre for Geosciences, Section 4.2: Geomechanics and Scientific Drilling, Telegrafenberg, 14473 Potsdam, Germany

[2] GMuG Gesellschaft für Materialprüfung und Geophysik mbH, Dieselstr. 9, 61231 Bad Nauheim, Germany

- Pairing of the hydrophone-like AE sensors with hydraulic equipment offers a simple yet effective means to improve the network geometry.

Keywords Acoustic emission monitoring · Piezo-electric sensor characterisation · Polarity · Recording ranges · STIMTEC experiment · Reiche Zeche underground research laboratory

1 Introduction

In 2018–2019, the STIMTEC hydraulic stimulation experiment was conducted at the Reiche Zeche underground research laboratory in Freiberg, Saxony/Germany, at a depth of about 130 m below the surface in metamorphic gneiss (Renner and STIMTEC-Team 2021; Boese et al. 2022). This experiment was designed to investigate the role of hydro-mechanical processes for the often-required enhancement of hydraulic properties of crystalline rocks in deep geothermal projects. Before, during and after the hydraulic stimulations of STIMTEC, we monitored the acoustic emission (AE) activity (seismic events typically with magnitudes $M_W \leq -2$) using a network consisting predominantly of piezoelectric AE sensors and high-frequency accelerometers. A double packer assembly was used to stimulate ten 0.7 m-long intervals along the 63 m-long, 15° dipping injection borehole (Fig. 1a). We applied the same injection protocol to each interval, yet we observed significant small-scale variability in the seismic and hydraulic responses to stimulation, as well as breakdown and instantaneous shut in-pressures (Adero 2020; Boese et al. 2022). While AE activity was high in the upper part of the injection borehole, no AE events were detected in its deepest part, ending in a high-permeability damage zone (Boese et al. 2022; Jiménez Martínez 2021). These observations raised questions concerning limits to AE event detectability throughout the stimulated volume, as average station distances increase systematically from shallow to deep stimulation intervals (from 18 to 30 m on average) along the injection borehole. In addition, attenuation estimates as determined from lab experiments on core samples showed higher attenuation in the vertical compared to the horizontal direction (Adero 2020). The latter was attributed to the strong sub-horizontal foliation of the Freiberg gneiss (e.g. Vervoort et al. 2014). Given the dip of the injection borehole, seismic waves from the deep stimulation intervals to the monitoring stations propagate rather vertically through the rock volume. To investigate potential detection issues, an AE sensor installed like a hydrophone (HAE) was placed into the down-dipping, water-filled hydraulic monitoring borehole (previously used for pressure monitoring only) during the final phase of the STIMTEC experiment (Fig. 1a).

During the follow-on STIMTEC-X experiment in 2020–2022, we installed HAE-sensors in up to six down-dipping boreholes close to the stimulation intervals aiming to improve coverage and reduce detection thresholds (Fig. 1b). We often paired the HAE sensors with hydraulic equipment, like the double packer probe. To ensure the best possible seismic monitoring of selected borehole intervals, we rearranged the HAE sensors for each measurement configuration anew surrounding the stimulated interval, with at least one at distances of ~ 3–4 m. Six pneumatically-coupled AE sensors and four accelerometers remained fixed at their positions at all times. In the following, we refer to this temporary hybrid network layout as an adaptive monitoring network.

At the field scale, conventional hydrophones have been used successfully in boreholes in addition to geophones for different monitoring applications. Conventional hydrophones are insensitive to vibrations because they do not measure particle motion but rather fluid pressure fluctuations in fluid-filled boreholes in response to radial deformation of the borehole wall by passing seismic P- and S-waves (White 1953). Therefore, they do not require coupling to the borehole wall and are easy to install in water-filled boreholes. Ikeda and Tsukahara (1983) first reported on using hydrophones in addition to AE sensors during hydraulic fracturing for stress measurements in two boreholes in Japan. Gibowicz et al. (1991) and Phillips (2000) used hydrophones in combination with accelerometers and geophones to derive focal mechanism solutions of induced seismic events at the underground research laboratory in Manitoba, Canada and for hydraulic stimulation of the geothermal reservoir in Soultz-Sous-Forêts, France. High-frequency hydrophones were used during the EGS Collab experiment at the Sanford Underground Research Facility to monitor stimulation experiments at the decametre scale (Schoenball et al. 2020).

The HAE sensors used in this study are conventional piezoelectric AE sensors optimized for in-situ experiments and manufactured for cementing the sensors in water-filled boreholes. Installing the sensors loosely in water-filled boreholes without cementation or a (pneumatic) coupling system makes the sensor a hybrid sensor between a pressure-sensitive hydrophone and an AE sensor sensitive to elastic deformation. When hanging in the fluid column they record pressure waves but when in contact with the borehole wall

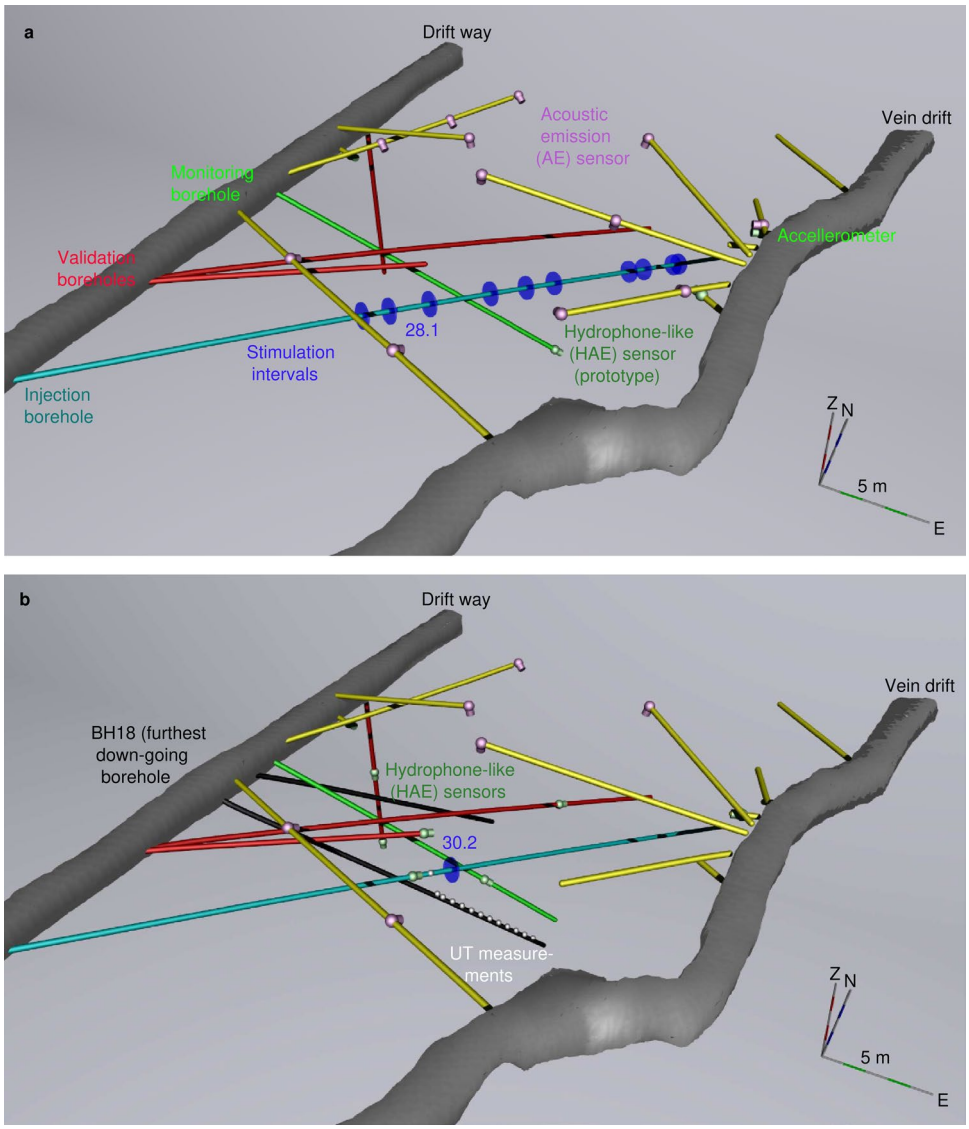

Fig. 1 **a** Three-dimensional view of the stationary monitoring network installed in July 2018 during stimulation of interval 28.1 m borehole depth during the STIMTEC experiment at the Reiche Zeche underground laboratory in Freiberg, Saxony/Germany. The two access galleries are the straight north–south trending driftway and the curved vein drift. Hydraulically stimulated intervals along the injection borehole (BH10, cyan) are shown schematically as blue rings. AE sensors (light purple) and accelerometers (light green torches) are located in upwards-directed monitoring boreholes (yellow) above the down-dipping injection borehole and other boreholes (red and green). The hydrophone-like AE sensor was added for testing in November 2019. **b** Example of one realisation of the adaptive monitoring network during stimulation of the interval 30.2 m borehole depth in October 2020 during the STIMTEC-X experiment. Some of the AE sensors were replaced by hydrophone-like AE sensors (green torches), placed in the down-dipping boreholes, previously used for hydraulic monitoring. Two new down-dipping boreholes (black) were drilled as part of STIMTEC-X of which the southernmost (BH18) extends furthest below the site. Also shown are source location positions for ultrasonic transmission (UT) measurements in the injection borehole and BH18 (Color figure online)

they are also sensitive to elastic waves. Therefore, the sensor response is not directly comparable to conventional hydrophones used in exploration geophysics. Nevertheless, installing waterproof and pressure-resistant AE sensors like hydrophones instead of cementing them, provides similar installation advantages in boreholes as conventional hydrophones. Earlier prototype versions of the sensor used in STIMTEC have been successfully implemented by cementing into boreholes in other in-situ experiments, e.g. the earthquake nucleation experiment JAGUARS in South Africa (Plenkers et al. 2010, Kwiatek et al. 2011), the SATREPS experiment (Moriya et al. 2015; Naoi et al. 2015a, b) and the Bedretto Reservoir Project Valter (Plenkers et al. 2023).

To investigate the limits to AE event detection in the deepest part of the STIMTEC injection borehole we installed HAE sensors in the surrounding water-filled boreholes. The sensors were either hanging freely in the water column, were attached to hydraulic tubing or they were lying on their side in contact with the borehole wall in water-filled down-dipping boreholes. Cementing the sensor was not an option during the STIMTEC and STIMTEC-X experiments because boreholes needed to stay accessible and open for other measurements. We report here on the seismic monitoring performance of the HAE sensors evaluated from active and passive seismic monitoring. We discuss the following sensor performance measures, which we consider important for the application of the HAE sensor for the purpose of monitoring cm- to dm-scale deformation associated with hydraulic stimulations at the decametre scale:

- Sensitivity (including incidence angle-dependence of the amplitude) and frequency bandwidth of the sensor (including resonance frequencies);
- Coupling (including effort to achieve good coupling and arising issues);
- Placement (including ease of installation and re-installation, combination with other sensors);
- Polarity (including onset characterisation).

The instrument response of piezoelectric AE sensors (including HAE) is complex because the amplitude response is not flat over their frequency bandwidth due to sensor-specific resonant frequencies (Ohtsu and Aggelis 2022; Plenkers et al. 2022) and it depends on the placement and coupling of the sensor. We compare these performance measures for the HAE sensors and pneumatically-coupled side-view AE sensors, by reporting on practical aspects resulting from these parameters, such as signal-to-noise ratios (SNR) and recording distances given the site characteristics, the sensor's ability to record S-phases and their usability in combination with e.g. hydraulic equipment.

Our analysis is motivated by the wish to detect, locate and derive focal mechanism solutions for small-size ($M_W \sim -3$) AE events, requiring good spatial 3-D sensor coverage and accurate locations of the AE events. Therefore, we compare the obtained location accuracy and assess the advantages as well as disadvantages of using stationary and adaptive monitoring networks for monitoring hydraulic stimulation campaigns and characterisation of AE events.

2 Data and Methods

The sensors used in this study use the piezoelectric effect to measure deformation introduced by the propagation of elastic waves (e.g. Plenkers et al. 2022). Piezoelectric sensors operate in near-resonance mode, and come in a large variety of sensor types for both the kHz and MHz range. For in-situ experiments AE sensors available on the market target different monitoring applications typically in the frequency range between 1 kHz and up to 200 kHz. When properly coupled to the rock mass, these sensors are able to record high-frequency elastic waves with high sensitivity (an overview on in-situ experiments with AE sensor recording is provided by Plenkers et al. 2022). The sensor's in-situ response at high frequencies depends on the quality of the sensor's coupling to the rock mass. Contrary to classical pendulum-based sensors such as geophones or accelerometers, these piezoelectric sensors require in-situ calibration to actual ground motions, which is not easily determinable, making relative calibration methods the only way to determine the sensor's transfer function to ground motions (see e.g., Kwiatek et al. 2011; Naoi et al. 2014; Villiger et al. 2020; Plenkers et al. 2022).

The STIMTEC experiment was seismically monitored using a stationary network, comprising twelve side-view AE sensors, three accelerometers and one broadband sensor (see Boese et al. 2022 for details). The AE sensors of type *GMuGMABLr-7-70* comprise a piezoelectric disk of PZT ceramic and were located in dry (sub-horizontal or upgoing) boreholes above the stimulation borehole and pneumatically pressed to the borehole wall. The main resonance of these sensors is at about 70 kHz. Uniaxial Wilcoxon 736T accelerometers were mounted onto a plate and glued to the rock mass at the polished bottom of 1–2 m-long boreholes (using the two-component JB Weld epoxy). All accelerometers were co-located with AE sensors for calibration purposes. An HAE sensor was added to the network for the final phase of the experiment, the prototype *GMuG HAE40k* (Fig. 1a). According to the manufacturer, the sensor has a resonance frequency close to 35 kHz. This sensor is waterproof and pressure resistant to pressure up to 1 MPa. The HAE sensor was lowered to the bottom of the down-dipping hydraulic monitoring borehole to provide a sensor in close proximity (6–17 m) to deeper stimulation intervals (Fig. 1a). We exploratory tested the HAE sensor's application without optimal coupling (coupled through the borehole fluid and the contact with the borehole wall). It was not known which wave first arrives at the HAE sensor, the waves traversing the water in the borehole or elastic waves from the surrounding rock.

In the STIMTEC-X experiment, we replaced six AE sensors of type *GMuG-Ma-BLr-7-70* with six HAE sensors

(Fig. 1b). One of these was the prototype used during STIMTEC, and the other five were of type *GMuG-Ma-Blc-30-35*, developed from the prototype *GMuG-HAE40k*. Sensor *GMuG-Ma-Blc-30-35* are pressure resistant to 10 MPa and also have the main resonance at about 35 kHz. Differences between the prototype HAE and the new HAE sensors are shown in Supplementary Information Figures S1 and S4. Without cementation, the relative ease of installation (attached to hydraulic tubing, freely hanging in the water column of a vertical borehole or lying on its side in contact with the borehole wall in inclined boreholes) allowed a flexible placement of these HAE sensors during the course of the experiment. For each stimulation interval anew, the HAE sensors were placed in the closest available boreholes. If no other instrumentation was in these boreholes HAE sensors were typically installed at half depth or total depth of the down-dipping boreholes. Otherwise, they were paired with hydraulic pressure gauges or the double packer probe used for localized injection to make best use of the existing infrastructure. In the latter cases, HAE sensors were installed a few meters above the other equipment, allowing us to instrument the majority of the down-dipping boreholes with one sensor each. The water level of the down-dipping boreholes was checked before each field campaign and boreholes were regularly refilled with water.

We focus this analysis on the performance of the HAE sensor located above the double packer probe as seen from stimulations in six different boreholes. For this configuration, the HAE sensor poses a simple but effective means to significantly improve AE event detection and localisation during decametre-scale hydraulic stimulations. We recorded full seismic waveforms of passive AE signals from the hydraulic stimulations (i.e. induced AE events), as well as active ultrasonic transmission (UT) measurements and centre punch hits with forces of 130–250 Nm in trigger mode at sampling rates of 1 MHz during the STIMTEC and STIMTEC-X experiments. P- and S-wave arrivals from passive AE signals were automatically identified using the algorithm of Wollin et al. (2018) as described by Boese et al. (2022). UT measurements were acquired along the length of the boreholes that were hydraulically stimulated and used for velocity model determination (Boese et al. 2021, 2022) as well as to investigate attenuation characteristics (Blanke et al. 2023). The ultrasonic transmitter *GMuG- Blr-Tr40* generates a repeatable signal by a rapid voltage discharge. UT source signals recorded by AE sensors at Reiche Zeche have a central frequency of ~ 20–30 kHz and are automatically stacked from a total of 1024 pulses to improve the SNR. Arrival times of the P- and S-waves, as well as the origin time of the UT source pulses were identified manually. From a total of 434 UT measurements, 314 were recorded during the STIMTEC (Boese et al. 2021) and 120 during the STIMTEC-X experiment (see e.g. Figure S2 of Supplementary information and data supplement). From the latter 474 P-picks were identified for HAE sensors and from the combined UT sets 2858 for pneumatically-coupled AE sensors, respectively. Of the total of 3332 P-picks approximately two-thirds (2058) have polarities identified by the automatic routine that is also applied to the AE events.

2.1 Amplitude Sensitivity with Incidence Angle and Recording Distance

We investigate changes in sensor sensitivity with the incidence angle of the piezoelectric sensors by analysing the records of 12 (from a total of 25) UT measurements from locations obtained along the borehole that reaches the furthest downwards (BH18, Fig. 2a). Sensitivity of side-view AE sensors like the pneumatically coupled-once used in this study, is highest in the direction in which the sensor is facing and declines for incidence-angles > 50° before the sensitivity increases again for incident angles > 90° (Manthei et al. 2001). The active source signals were recorded by the AE and HAE sensors located above the UT source (Fig. 2a). For this configuration, we achieved incidence angles < 50° by a sensor pair of an AE sensor (AE07) and an HAE sensor (H12Z). We compare amplitude (and polarity) characteristics of the direct P-wave arrivals in windows of 0.15 ms (150 samples) for these sensors.

There were no co-located HAE and AE sensors during the STIMTEC-X experiment. To investigate sensor differences, we analyse the SNR of P-arrivals versus recording distances for the bulk of all UT measurements. A wide range of incidence angles is obtained at specific source-receiver distance for the bulk of all UT data. Therefore, we consider the SNR values representative of the overall sensitivity difference between the two sensors. The SNR is determined as the ratio of the average signal amplitude in a 3.60 ms noise and 0.67 ms signal windows, respectively, in the time domain. We calculate the SNR of the unfiltered waveforms for the UT measurements (because signals are already stacked) and 3–28 kHz filtered waveforms for AE events (to separate the AE signal from the low-frequency injection noise). We compare the SNR of the P-waves for recording distances ranging between 2.6 and 35.7 m given the initial site characteristics (coda Q_S-values of 50–200 for the frequency range 5–20 kHz, see Fig. 4 by Blanke et al. 2023). We calculate regression lines to fit the 95th percentile of the data in 2 m distance bins for HAE sensors installed on the tubing as well as side-view AE sensors (in pairs when two have similar incidence angles and distances).

2.2 Sensor Coupling Performance

We investigate sensor coupling by analysing the power spectral density (PSD) of the background noise recorded

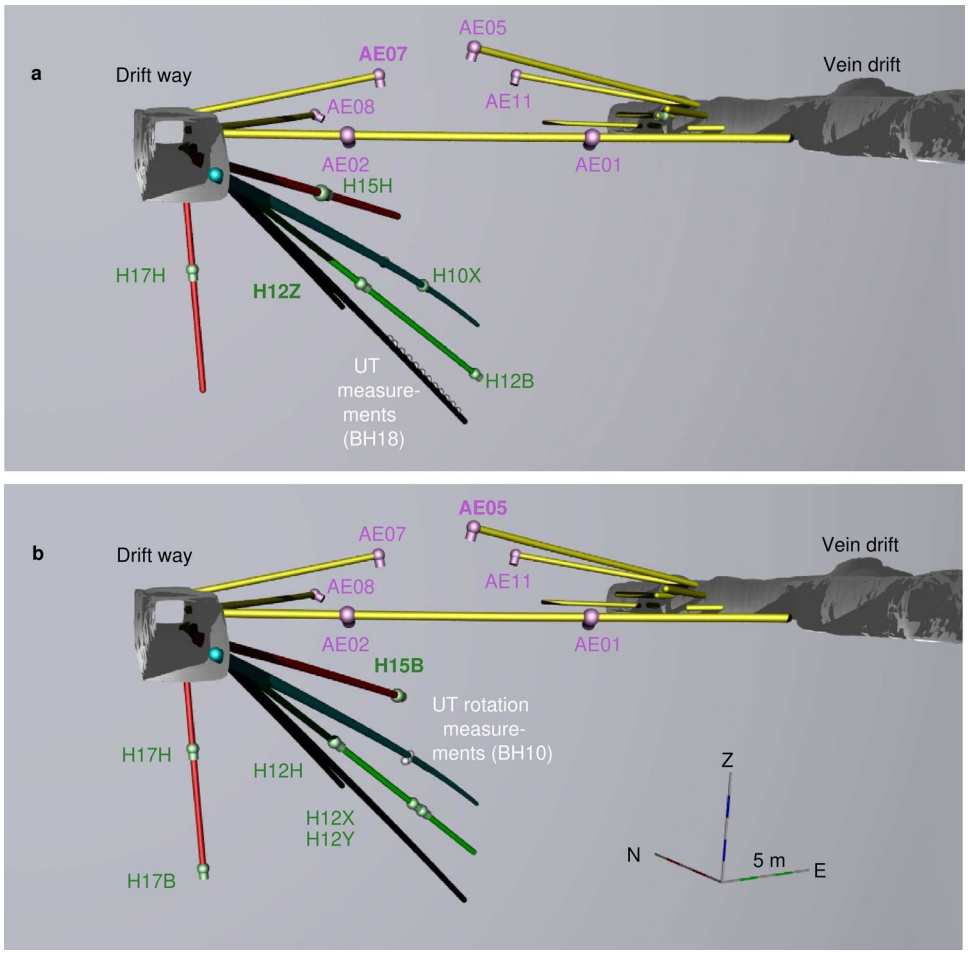

Fig. 2 **a** Network configuration during the STIMTEC-X active UT measurements along the lower part of BH18 in side view (looking towards north along the direction of the straight drift way tunnel). **b** Network configuration during the STIMTEC-X UT measurements at 27.9 m depth in the injection borehole in side view. Sensors are labelled 'AE' for acoustic emission sensors and 'H' for hydrophone-like AE sensors. Waveforms for highlighted sensors are shown in Fig. 6 (Color figure online)

before active centre punch hits (130 and 250 N) generated at 24 fixed points in the access galleries (see Boese et al. 2022 for more detail) during different surveys conducted between 12 October 2020 and 03 March 2021 (Table S1 in Supplementary Information). We use these data sets because there were no other ongoing activities at the STIMTEC site during these surveys. All AE and HAE sensors are connected to the same recording system (GMuG-AEsystem), so the internal system noise is the same. We compare the stacked noise PSDs of 1–70 kHz Butterworth-filtered, multi-tapered windows of 6.4 ms (6445 samples) length of the noise obtained before the P-arrival of ten successive centre punch hits at each hit point. The PSDs were calculated using the matlab function *pmtm* with a time-bandwidth product input of 3.5, an FFT length of 8192, a sampling rate of 1 MHz and a confidence window of 0.99. The resulting PSD amplitude estimate was scaled, so that the energy in the time and frequency domain is the same.

In the stacked noise PSDs, we look for common spectral peaks of sensors of the same type, that may reflect resonance frequencies. Since HAE sensors were either lying on their side in the borehole, hanging in the water column or were attached to hydraulic tubing, we look for differences between the noise PSD peaks for these different installations. Sensor coupling is considered to have the largest influence at high frequencies. However, investigating coupling is difficult to obtain and may reflect the resonances of tube waves for HAE sensors. Noise PSDs of HAE and side-view AE sensors are compared for their high-frequency content for the same surveys to identify temporal site-specific noises.

2.3 Sensor Polarity Characteristics

We focused our polarity analysis on 14 UT measurements during which the ultrasonic transmitter was rotated in 30° intervals (including some repeats) at a depth of 27.9 m in the injection borehole (Fig. 2b). We report these orientations as clock-equivalent orientations with upwards corresponding to noon (1200) and downwards corresponding to 6 pm (600). This set of UT measurements results in systematic changes in polarity and amplitude values. We compare polarity and amplitudes characteristics of the direct P-wave arrivals in windows of 0.15 ms (150 samples) from a nearby sensor pair of an AE sensor (AE05) and an HAE sensor (H15B, Fig. 2b). For this position, both sensors are located above the source point but at distances that differ by approx. 10 m

for AE05 and H15B, resulting in incidence angles of 18° and 77° at the sensors. Two other HAE sensors, H12H and H17H, are located at sub-horizontal distances of 4.6 and 14.6 m, with incidence angles perpendicular to the direction in which the sensors are facing (63° and 90°). These vertical and horizontal propagations correspond to the slow and fast propagation directions of the transverse isotropic velocity model describing the anisotropy at the site (Boese et al. 2022), controlled by the strong sub-horizontal foliation of the metamorphic gneiss rock.

These same UT measurements were also used to compare the prototype HAE and new HAE sensors, which were installed 1 m apart in the hydraulic monitoring borehole (H12X and H12Y; Fig. 2b) to assess their sensitivities and differences in travel times (see Supplementary Information Figure S1). Our intent was to investigate how potential misplacements of sensors due to re-installation could be resolved.

The recorded polarity and the character of the onset (impulsive versus emergent) are important for the determination of focal mechanisms. There are no differences regarding the electronic components of the recording setup between AE and HAE sensors. We compare the P-wave polarity of high SNR onsets (> 3) for the known polarity of the active UT source signals. We check this for different incidence angles.

2.4 Network Performance

To compare the performance of the different station networks during STIMTEC and STIMTEC-X, we compare the location accuracy obtained from AE events recorded by more than five sensors from adjacent stimulation intervals 28.1 and 30.2 m depth in the injection borehole (Fig. 1), stimulated during the STIMTEC and STIMTEC-X experiments, respectively. Stimulation involved a hydraulic fracture and three re-fracturing cycles as well as a step-rate test (cf. Boese et al. 2022). These central stimulation intervals are surrounded by all monitoring sensors (azimuthal gap 84° for STIMTEC and 71° for STIMTEC-X), the angle of incidence to the AE sensors is always < 50° (largest sensitivity of the piezo AE sensors, Manthei et al. 2001). We compare the obtained locations by analysing the normalised root mean square deviation, which best accounts for different event-station distances and is defined as

$$rmsdn = \sqrt{\left[\frac{\sum_i (t_i^{calc} - t_i^{obs})^2}{\sum_i (t_i^{obs})^2}\right]}$$

where t_i are calculated and observed travel times for the i stations.

The detectability of the network depends on the magnitude of the AE events. To check that the magnitudes of the induced events from the two stimulation intervals are comparable, we determine relative magnitudes by generally following the method of Eisenblätter and Spies (2000) but using only the amplitude data from the stationary, pneumatically-coupled AE sensors during both experiments. As transfer functions of AE sensors are not commonly known in-situ, AE amplitudes are not directly comparable to common seismological magnitude scales (e.g. Plenkers et al. 2022). We then calculated the relative AE magnitude M_{AE} according to

$$M_{\mathrm{AE}} = 20 log_{10}(A_{mean}), \tag{1}$$

with A_{mean} being the geometrical mean of all amplitudes A for the stationary AE sensors during both experiments with

$$A = A_0 \frac{r}{r_0} exp[\alpha(r - r_0)], \tag{2}$$

where A_0 denotes the amplitude of the P-onset in a 0.47 ms long window, bandpass-filtered with a causal filter in the frequency range 3–28 kHz, normalized to 1 µV signal amplitude at the sensor output, r the distance between AE event and respective sensor, r_0 a normalization parameter, roughly the mean distance between event and sensors and here set to 15 m, α the damping of the compressional waves, set to $\alpha = 0.028$ m^{-1} on a trial basis, corresponding to a quality factor Q_P of 150 at 7.5 kHz and $v_P = 5.6$ km/s. We assume that $Q_P > Q_S$ and an average Q_S of ~ 100 at 7.5 kHz and ~ 140 at 15 kHz was independently determined from coda Q analysis of the UT measurements from the injection interval (cf. Fig. 4 of Blanke et al. 2023.)

3 Results

We first show results for the performance measures of the HAE sensor before comparing the performance of the hybrid adaptive network and the stationary network.

3.1 Hydrophone-Like AE Sensor Performance

3.1.1 Signal-to-Noise Ratios and Recording Distances

The > 400 UT measurements obtained during the course of the STIMTEC and STIMTEC-X experiment allowed us to compare recording distances for the HAE sensors and AE sensors (Fig. 3). Good SNRs (SNR > 3) were recorded by the HAE sensors installed on hydraulic tubing for source-receiver distances up to 17 m. This value is likely determined by the high impedance contrast of the water-filled borehole ($Z_W = \rho V_p$ with $\rho = 1000$ kg/m^3, $V_p = 1500$ m/s) and the host rock ($Z_R = \rho V_p$ with $\rho = 2700$ kg/m^3, $V_p = 5600$ m/s), resulting in an estimated transmitted energy flux ratio ($E_T/E_I = T^2 Z_W/Z_R$ with $T = 2Z_R/(Z_W + Z_R)$) of 32% at normal incidence angles to the borehole. This value decreases steadily the more inclined the angles are compared to normal to the

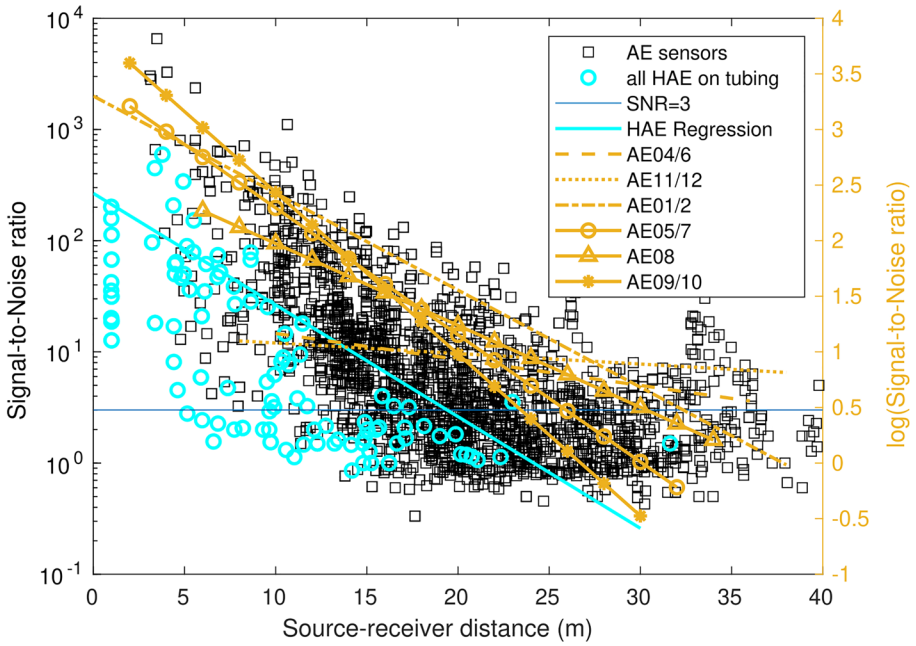

Fig. 3 Signal-to-Noise ratio (SNR) of ultrasonic transmission measurements for recording distances of hydrophone-like AE sensors installed on tubing (HAE, cyan circles) and pneumatically coupled AE sensors (black squares). Regression lines for the 95% percentile of all SNRs for pairs of AE sensors with similar incidence angles and all HAE sensors on tubing are shown by different lines (Color figure online)

borehole (cf. Figs. 2.6–12 of Stein and Wysession 2003). For most inclined incidence angles a significant portion of the incident S-wave is converted and transmitted as a pressure wave in the water-filled borehole (transmitted energy flux ratios of up to 45%). This theoretically allows for S-waves to be recognised in the water-filled boreholes as secondary pressure wave signals.

Despite the expected differences in absolute amplitude for HAE sensors and AE sensors due to their different sensitivity in the frequency band of interest, the slope of the SNR decay with distance does not differ systematically between both sensor types. In general, noise levels are comparable for HAE sensors and AE sensors, with the exception of the HAE sensor attached to the double packer probe, often displaying an elevated noise level (see Fig. 4 and next section). To achieve a fair comparison considering the installation of the HAE sensors, we determine the SNR-distance values only for those HAE sensors installed on hydraulic tubing (Fig. 3). These HAE sensors are not in contact with the borehole wall, so they record pressure waves. We also checked the SNR decay with distance for other HAE sensor installations as is shown in Fig. S3a) in the Supplementary Information. We observe that the contact with the borehole wall either through the side of the sensor (H1xH, sensors installed at half depth of the borehole) or side and face (H1xB, sensors installed at the bottom of the borehole, where x denotes the borehole number) leads to larger SNR-values with distance compared to the HAE sensors installed on hydraulic tubing but smaller than the SNR-values from pneumatically-coupled AE sensors.

SNR values are expected to show a systematic decline with source-receiver distance due to geometrical spreading and attenuation. We tested whether correction for attenuation and geometrical spreading (assuming $Q_P = 150$ and 1/R decline with distance R) removes the observed decay in amplitude data (Supplementary Information Fig. S3b). We found this did not fully explain the amplitude decay observed with recording distance. Therefore, the installation type and the sensor's sensitivity are dominant factors controlling signal detection ranges.

3.1.2 Performance of the Hydrophone-Like AE Sensor on the Double Packer

Some HAE sensors were attached to hydraulic tubing above the double packer probe used for localized injection for stimulations in six boreholes. For five of these boreholes this worked well, i.e. the HAE sensor attached to the hydraulic tubing picked up seismic signals comparable to the signal recorded by the other HAE sensors. We show in Fig. 4 an example of an AE event recorded by multiple HAE sensors at comparable source-receiver distances, where H12Y is the HAE sensor attached to the double-packer in the hydraulic monitoring borehole. The calculated SNR of the P-arrival for bandpass-filtered waveforms (3–28 kHz, to separate the AE signal from the low-frequency injection noise) is 1.3 for H12Y compared to 4.1 for H10X and 3.7 for H15B for the example shown (see Fig. 2 for sensor locations). For

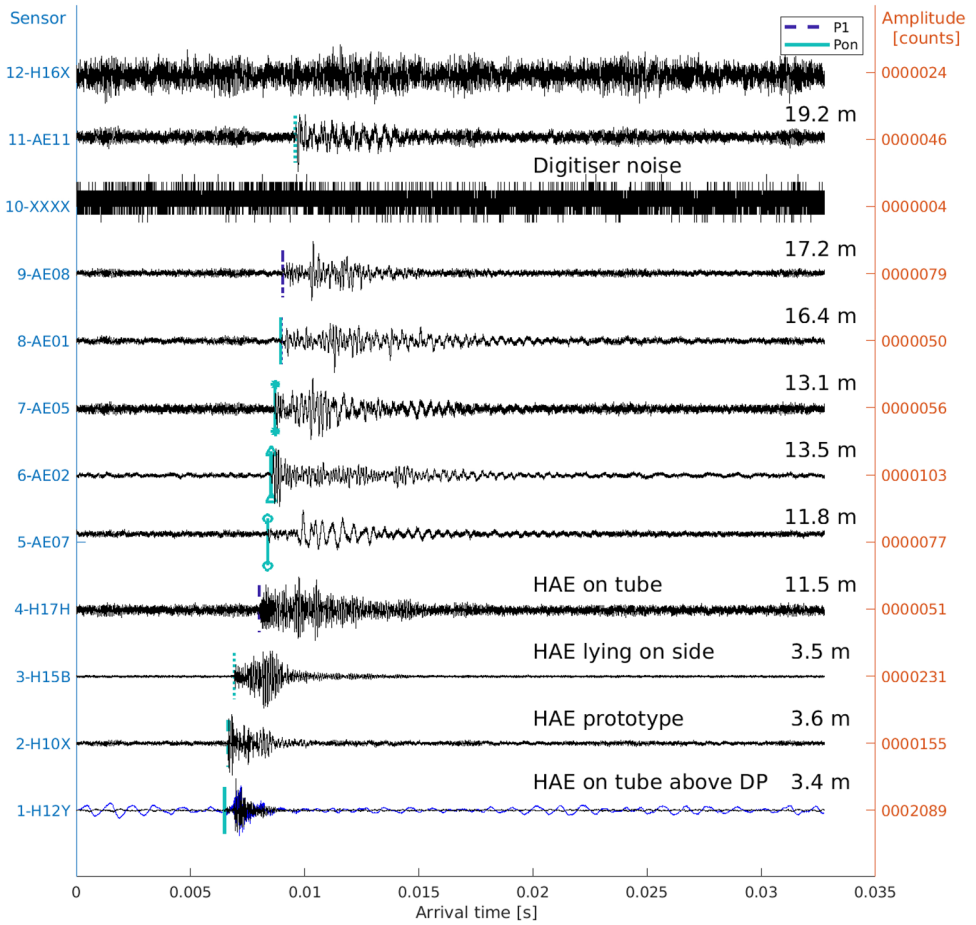

Fig. 4 Bandpass-filtered (3–28 kHz) waveform example of an AE event occurring during stimulation of interval 14.9 m depth in the hydraulic monitoring borehole recorded by the HAE sensor attached to the double packer probe (H12Y), and at comparable distances (as stated on the right) by other HAE sensors (prototype *GMuG HAE40k* at H10X and *GMuG-Ma-Blc-30-35* at H15B, H17H, and H16X) and common AE sensors (AE01–AE11). This bandpass was chosen because it effectively removes the noise caused by stimulation on the HAE sensor H12Y above the double packer probe (as shown for H12Y with the unfiltered trace in blue), wich none of the other sensors exhibit. The installed accelerometers did not record this AE event and are, therefore, not shown. See Fig. 2a, b for sensor locations. P-arrivals are marked as light blue bars where polarity could be identified and dark blue bars when not. The traces shown here are normalised to the maximum amplitude (in counts as shown on the right side) (Color figure online)

the sixth borehole (BH18), the HAE sensor (H18Y) was attached to hydraulic tubing 3.10 m above the centre of the double packer probe and it did not record any of the AE events occurring during the stimulation of the interval 12.7 m depth in BH18. During stimulation of this interval, the noise floor and signal frequency content of the induced AE events were not different compared to other stimulation intervals. The lack of this HAE sensor to record the induced AE events can be explained if the sensor above the double packer was not submerged in water because of a natural high-permeability fracture situated above the stimulation interval but below the HAE sensor. Records of the water level in BH18 revealed a rapid drop (few minutes) in water level after the borehole was filled up to a borehole depth of approximately 12.5 m. Therefore, the HAE sensor (at a borehole depth of 9.6 m) did not record any of the AE events, because it was not surrounded by water. We conclude that the presence of fluids is necessary to couple the HAE sensor attached to hydraulic tubing.

3.1.3 Coupling and Resonance Frequencies

Coupling of the HAE sensor to the rock mass is provided through the fluid in the borehole and through the direct contact of the sensor with the borehole wall. We did not investigate the HAE sensor performance in dry boreholes to check if contact with the borehole wall might be sufficient for coupling the HAE sensors as we only tested installing HAE sensors in inclined water-filled boreholes. From stacked noise PSDs of active measurements from different centre punch surveys (Fig. 5 and Supplementary Information Fig. S4), we observe a broad resonance

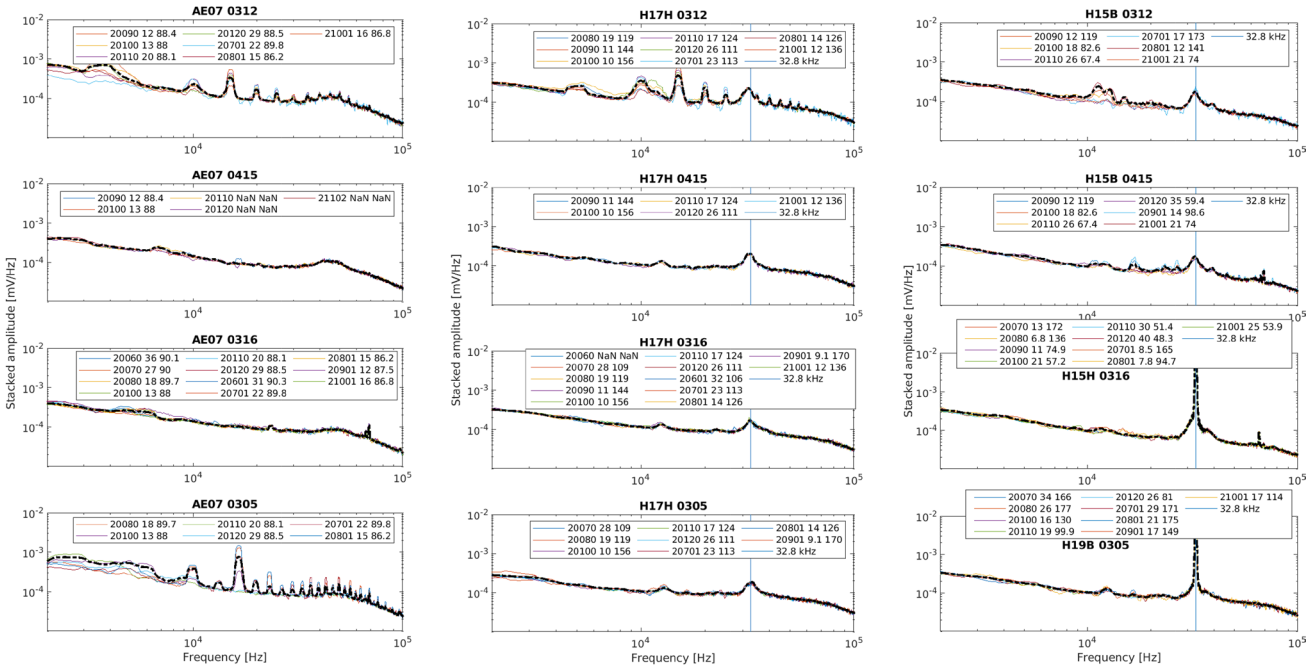

Fig. 5 Comparison of stacked noise PSD with frequency from four active seismic centre punch surveys for a single pneumatically-coupled, side-view AE sensor and different HAE sensors (as listed in the title of each panel). HAEs shown here are installed at half-depth (H1xH) or bottom of the boreholes (H1xB, where x marks the borehole number). The average spectra from all hitpoints of one survey are shown in black. Note that some frequency peaks change with time, likely reflecting variable noise conditions during the surveys. The legend displays hitpoint location, source-receiver distance (in m) and incidence angle (°) for the named sensor (Color figure online)

peak with a maximum at 32.8 kHz for all HAE sensors reflecting the main eigenfrequency specific to the PZT ceramic elements of these HAE sensors. We also distinguish a secondary peak at 12.3 kHz for the HAE sensors that seem to be characteristic of the HAE instrument, because it is not seen for the side-view AE sensors (e.g. AE07 in Fig. 5). Many smaller narrower peaks at 9.7–10.0, 15.0–15.1 or 16.4, 19.8–20.2 and sometimes also at 13.1 and 23.8–24.0 kHz for some of the HAE sensors are also observed on nearby accelerometers and side-view AE sensors (Supplementary Information Fig. S4), so they may reflect variable noise conditions at the site during the surveys rather than sensor-related resonances.

3.1.4 Onset Picking Performance

We observe similar residual distributions for the manually identified P-wave arrivals of the UT measurements for all sensors, suggesting that first arriving waves recorded by HAE sensors can be accurately picked despite emergent arrivals. The comparable residual distribution (Supplementary Information Fig. S5) likely results from HAE sensors having more emergent but higher frequency onsets versus the side-view AE sensors having more impulsive, low-frequency onsets (e.g. Fig. 6a) for similar incidence angles but different source-receiver distances of approximately 10 m.

3.1.5 Phase Polarity Characteristics

Polarity data from the active seismic UT data show opposite polarity for the majority of the HAE sensors compared to the side-view AE sensors (Fig. 6b). For source-receiver distances less than ~ 10 m, having the highest SNR values, we observe consistent downward polarity for the HAE sensors at all except two stations (Supplementary Information Fig. S6):

- H15H shows predominantly upwards polarity but only 22% of the observations has SNR > 3, likely because there is an elevated monochromatic noise level just before the identified P-wave arrival that may mask the true P-wave polarity;
- H16Z shows a mixture of different polarity arrivals (38% with SNR > 3), however, manual polarity checks show predominantly weak downward polarities, which are often misidentified by the automatic polarity picker that was applied to the manually identified phase arrivals (same as used also for AE event picking).

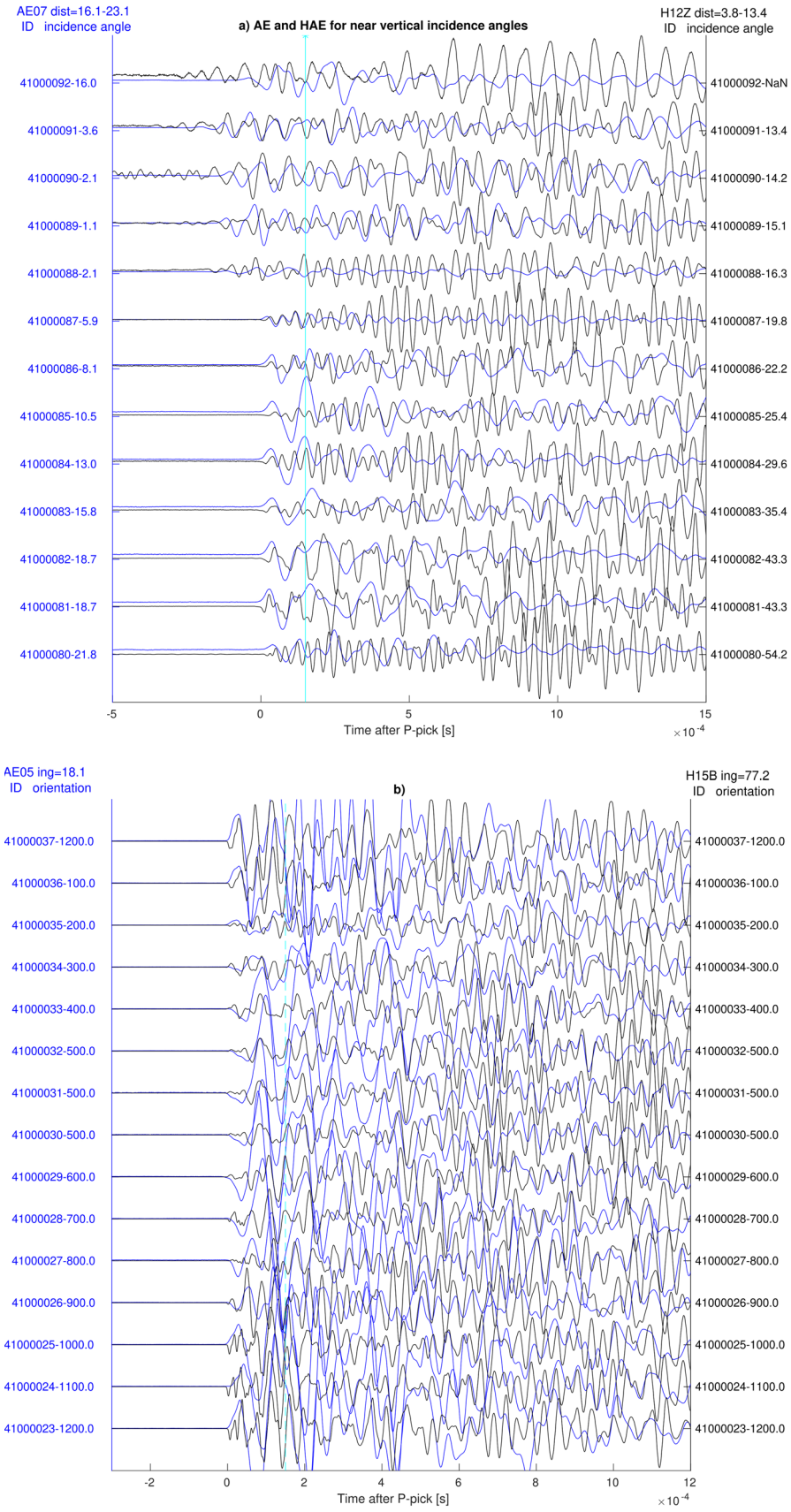

Fig. 6 **a** Waveform example with normalized maximum amplitude of records obtained with an AE-hydrophone H12Z (black) and a pneumatically-coupled AE-sensor AE07 (blue) for UT measurements in the deepest part of BH18 (borehole depth 18.4–29.4 m see Fig. 2a, distance range to sensors is stated above the panel). Both sensors recorded the near-vertical waves with small incidence angles as stated in the label after the event ID. **b** Waveform examples with normalized maximum amplitude of records obtained with an AE-hydrophone H15B (black) and a pneumatically-coupled AE-sensor AE05 (blue) for UT measurements, during which the transmitter was rotated in 30° intervals at a depth of 27.9 m in the injection borehole (Fig. 2b). The source orientation is given as a clock-equivalent orientation with an upwards pointing source for 12 o'clock (as stated in the label after the event ID. Note the opposite polarities of the two sensors. The light blue vertical line shows the window of 0.15 ms (150 samples) in which the amplitude was determined for Figs. 7 and 8 (Color figure online)

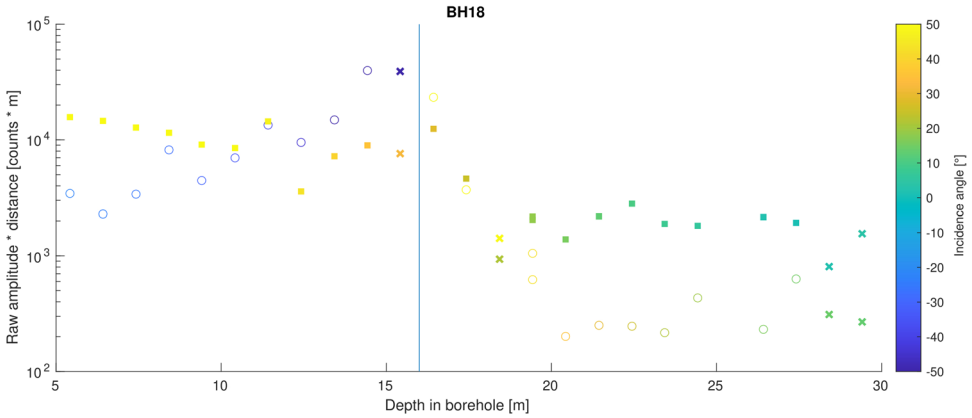

Fig. 7 Amplitude-multiplied-by-distance records of AE-hydrophone H12Z (circles) and AE-sensor AE07 (squares) versus depth position of the UT source in BH18. Source-receiver distances differ by approx. 10 m. From borehole depths > 18 m (vertical line, ID 041000080), incidence angles < 50° (Color scale) were obtained for both sensors (see also Fig. 6a). Incidence angles from the opposite direction in which the sensor is facing are displayed as negative incidence angles (angle-180°) for better visualisation. Filled or open symbols represent first motion polarity, crosses show where no polarity could be identified on the unfiltered traces (Color figure online)

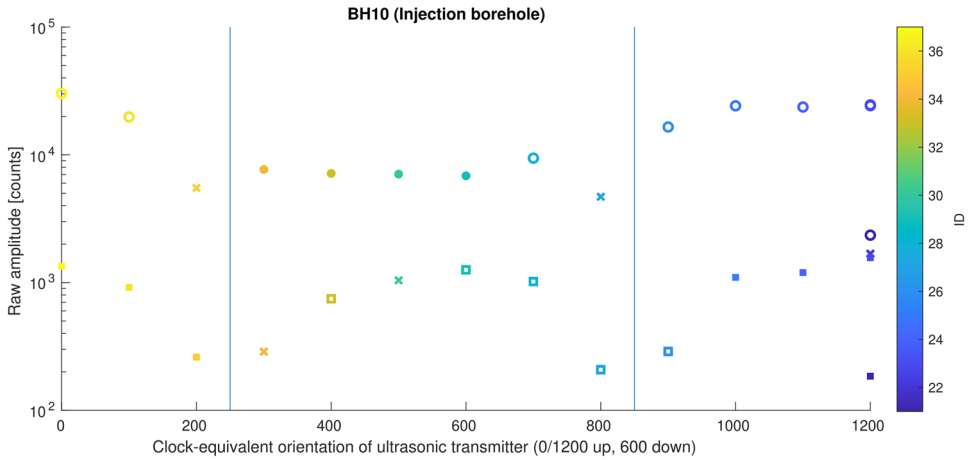

Fig. 8 Raw amplitude records of HAE sensor H15B (circles) and AE sensor AE05 (squares) versus clock-equivalent orientation of the ultrasonic transmitter, which was rotated in 30° intervals at a depth of 27.9 m in the injection borehole. The HAE sensor H15B and AE sensor AE05 are located above the source point at distances of 3.4 and 13.4 m and show the largest amplitudes for upwards-pointing source orientations (9 o'clock–1 o'clock). Colour reflects the last two digits of the event ID as shown in Fig. 6b. Open symbols represent dilatation at the sensors, whereas filled symbols represent compressional polarities (Color figure online)

Therefore, we do not consider the polarity readings from these two HAE sensors as they are unclear. The remaining other HAE sensors show predominantly a consistent polarity at least within 10 m of the source and for SNR > 3 (Supplementary Information Fig. S6). Figure 7 shows that the general P-wave amplitude characteristics of the HAE sensor are the same as for an AE sensor at different source-receiver distances above the UT source location. It also shows the opposite polarity of the two sensors, where filled symbols represent compressional motion at the sensor. The same is also observed for the rotating source at fixed source-receiver distances (Figs. 6b and 8). We also checked for systematic changes in the polarity pattern of the HAE sensors with incidence angle. We considered an incidence angle-dependent polarity as this is seen for conventional hydrophones (see also laboratory calibration in the Discussion). For incidence angles ≥ 25° we consistently see a reversal of polarity for the HAE sensor due to the internal construction of the sensor as observed in the field and lab compared to side-view AE sensors. There are few observations with incidence angles of < 25° (see e.g. H12Z for ID 041000086, Fig. 6a) often with weak onsets where the polarity might be the same as for the AE sensors. We also compared the polarity for

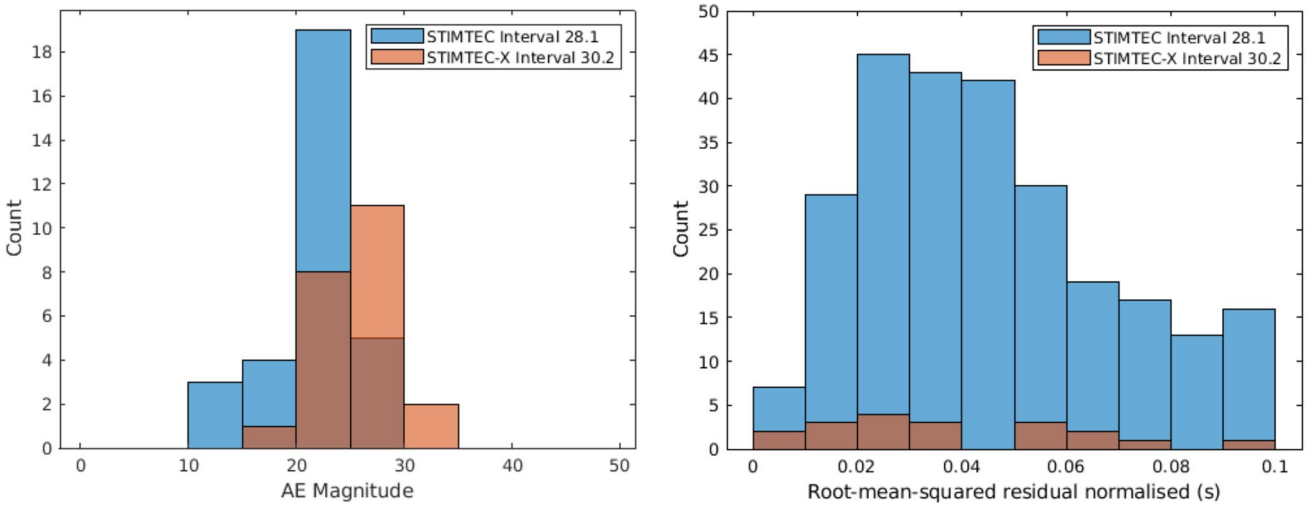

Fig. 9 Comparison of AE magnitude (**a**) and normalised rms residual distributions (**b**) of AE events located near interval 28.1 m depth in the injection borehole during STIMTEC (blue) and 30.2 m depth during STIMTEC-X (orange), displaying the improvement in detection and localization of induced AE events obtained using the adaptive seismic monitoring network. The absolute locations are shown in Fig. 10 and will be refined in the future using the double-difference approach (e.g. Waldhauser and Ellsworth, 2000) (Color figure online)

filtered waveforms of the HAE sensors (causal butterworth filter between 1 and 5 kHz, Supplementary Information Fig. S7) to make the frequency content comparable to that of the AE sensor, providing the same polarity results as the unfiltered waveforms.

3.1.6 Placement Accuracy

HAE sensors had to be deinstalled after each field campaign (e.g. surveys in Table S1). Given the flexible placement of the HAE sensors in the adaptive network approach, one concern was that the sensor position and characteristics change when the sensor is reinstalled, potentially influencing AE event location accuracy. To test whether slight placement differences can be detected and resolved using the active seismic UT data, we placed two HAE sensors spaced 1 m apart (the prototype H12X and H12Y; see Fig. 2 and Supplementary Information Fig. S1) in the same borehole. We observe travel-time differences of 0.5 ms (500 samples) for these sensors, suggesting that sensitivity to a position should be resolvable accurately to 0.04 m corresponding to 20 samples in travel time, which can be distinguished even for emergent arrivals. The repeatability of measurements by reinstalling HAE sensors at the same borehole depth will be tested further making use of waveform similarities of AE events compared for the stationary AE sensors and the HAE sensors.

Table 1 Location statistics of AE events recorded during stimulation of intervals 28.1 and 30.2 m borehole depth during the STIMTEC and STIMTEC-X experiments

Interval	28.1 (frac)	28.1 (refrac)	30.2
Total events	15	267 (first 22 analysed)	31
Events located	15	22	27
Average normalised rms	0.090	0.101	0.087
Average horizontal error (95%)	5.76	6.20	5.33
Average vertical error (95%)	7.61	8.31	3.34
Average number of P-phases	10	10	6
Average number of S-phases	8	7	3

3.2 Network Performance in Locating Induced AE Event Activity

We now evaluate how the use of the adaptive network during the STIMTEC-X experiment improved the location accuracy of the AE events in comparison to the stationary network setup used during STIMTEC. Since we do not have sufficient data from a single injection interval for both campaigns, we analyse data from the adjacent stimulation intervals 28.1 (stimulated during STIMTEC) and 30.2 m depth (stimulated during STIMTEC-X) in the injection borehole (Fig. 1). The average distance in-between AE events in these two intervals is 4.2 ± 3.9 m, suggesting that source-receiver ray paths are similar. While less events were induced during stimulation

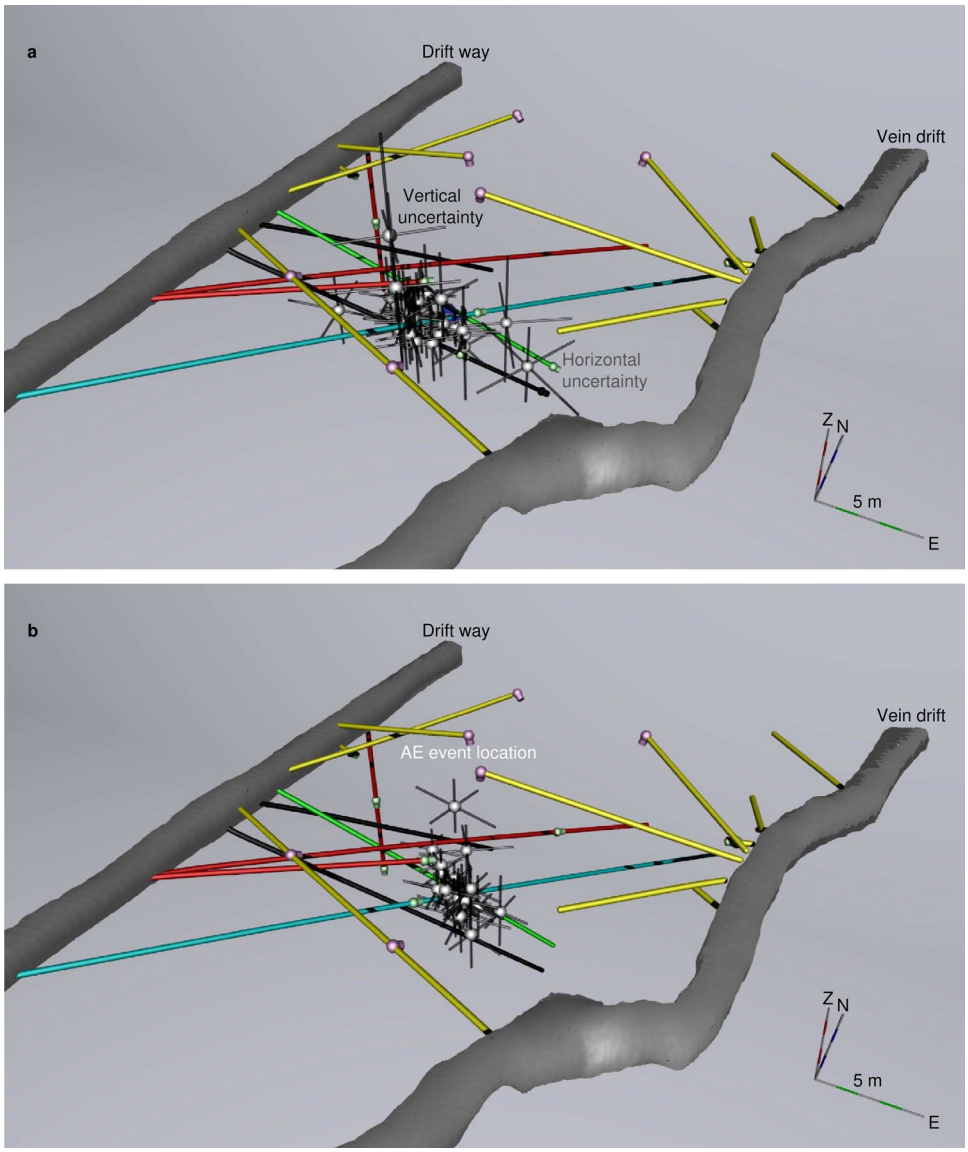

Fig. 10 AE event activity recorded during the STIMTEC (**a**) and STIMTEC-X experiments (**b**) in adjacent stimulation intervals (28.1 m and 30.2 m borehole depth) in the injection borehole. Uncertainty estimates in the horizontal and vertical directions are shown for the 68% confidence interval of the location estimate. Note that the events of stimulation interval 30.2 m have smaller uncertainty estimates (especially in the vertical direction) and are less scattered, despite being recorded by less monitoring sensors on average (Table 1) (Color figure online)

of interval 30.2 m borehole depth, their magnitudes are distributed in the same magnitude range as observed during stimulation of interval 28.1 m depth (Fig. 9a) as observed from relative magnitudes of AE events recorded by stationary side-view AE sensors during both experiments. In general, the stimulation of interval 28.1 m depth resulted in significantly more AE events than for interval 30.2 m depth (> 800 compared to 31, respectively). To compare similar numbers of AE events, we analyse only the AE events during the hydraulic fracture and first re-fracturing stage of the stimulation of interval 28.1 m (14 and first 22 of the 267 events), while we take all AE events from the whole sequence including the step-rate test of interval 30.2 m depth.

In Table 1 we compare average parameters obtained from locating all AE events per stimulation interval. We also compare the number of recorded S-phases for the AE events and obtain significantly fewer S-phases for stimulation interval 30.2 m compared to 28.1 m borehole depth. For the stationary network setup with pneumatically coupled AE sensors during STIMTEC we observe average values of 4.6 ± 2.9 m and 2.5 ± 1.0 m for maximum and minimum axes of the 68% uncertainty ellipse for interval 28.1 m depth in the injection borehole during STIMTEC. Using the hybrid network setup, we achieved significantly better values of 2.4 ± 1.2 m and 1.4 ± 0.3 m for maximum and minimum axes of the uncertainty ellipse for interval 30.2 m depth (Fig. 10). This is also seen when the standard rms travel-time residuals are compared between the two network setups. However, for an unbiased comparison of the travel-time residuals of events from these two intervals, we calculate the normalised rms residual (Fig. 9b), which better considers the differences in sensor-AE event distances. This is comparable for both intervals (Fig. 9b).

Table 2 Comparison of important sensor and monitoring parameters for AE sensor networks and hybrid networks

Comparison	AE sensor network	Hybrid (AE & hydrophone-like AE sensor) network
Common frequency band	1–60 kHz	1–40 kHz (limited by hydrophones)
recording distances/amplitude (based on active seismic UT measurements)	Up to ~ 30 m/high	Up to 17 m/reduced due to the impedance contrast of borehole rock and fluid and the type of installation
Optimal placement to stimulated intervals	Limited	Possible
Permanent installation	Possible in dry boreholes, only possible in wet boreholes by cementing	Not possible (sensors fail for elongated time periods in water) without cementing
Flexible installation (change in position and later reinstallation)	Laborious and limited due to installation on rods and coupling issues	Simple if non-optimal coupling is acceptable
Borehole use	Limited to AE sensors	Possible combination with hydraulic instrumentation
S-wave detection	Good	Limited
Coupling to borehole wall/resonances	Problematic/resonances site specific	No known issues/resonances due to strong tube waves possible
Polarity	Same for frontal and sideways incidence	Same for frontal incidence as AE sensors, reversed for incidence from the side

4 Discussion

In Table 2, we summarise and compare relevant sensor and practical parameters for monitoring networks comprising only AE sensors (as utilized during STIMTEC) as opposed to combined AE and HAE sensor networks (hybrid network as during STIMTEC-X). Selected important aspects highlighting advantages and disadvantages of using HAE sensors are discussed below.

4.1 Amplitude Sensitivity with Incidence Angle and Recording Distance

The observed differences in the decay of the SNR with recording distance for the different piezoelectric sensors for active UT measurements are not fully explained by geometrical spreading and attenuation given the site characteristics (Supplementary Information Fig. S3b). HAE sensors have a more limited bandwidth and show on average five times smaller SNR values compared to the AE sensors for UT signals at source-receiver distances up to 17 m. For the purpose of monitoring induced AE events at the STIMTEC site, the limited frequency range of the HAE sensors is sufficient, as AE signal spectra drop off to the noise level for frequencies exceeding 30 kHz likely due to damping. UT source signals generally contain more high frequencies up to 60 kHz.

We observe that the slope of the amplitude decay with distance is the same for HAE and AE sensors but maximum recording distances are shorter for HAE sensors, especially if installed attached to hydraulic tubing. We show that HAE sensor installation influences the overall decay of SNR with recording distances (Supplementary Information Fig. S3a). The AE sensors are installed above the stimulation intervals facing towards the AE event activity (resulting in low incidence angles at the sensors), that optimizes their sensitivity to ground motions for P waves. The HAE sensors are located close to the stimulation intervals in down-dipping boreholes, which—given the geometry of the network setup—results in high incidence angles (being more optimal for recording S waves; Supplementary Information Fig. S2). The sensitivity of HAE sensors is largest in the axial direction, but there are few observations for small incidence angles with respect to the HAE sensor axis, so the unfavourable geometry likely affects the observed HAE sensitivity. Other factors are the (incidence angle-dependent) impedance contrast and the coupling. The impedance between the rock mass and water-filled borehole causes a drop in the transmitted energy flux of elastic P-waves and a conversion of S-phases into pressure waves in the water-filled borehole. The HAE sensors installed on tubing and recording only pressure waves have the lowest SNR and fastest SNR decay with distance. When the HAE sensors are in contact with the borehole wall higher SNR amplitudes over larger distances are observed likely because elastic waves are recorded in addition to pressure waves.

4.2 Coupling and Resonance Frequencies

Sensitivity is intrinsically linked to coupling, which is problematic to assess properly in the field because we did not have co-located HAE and AE sensors. We do not observe obvious resonance frequencies for HAE sensors that differ from those at nearby AE sensors other than the sensor's "eigenfrequencies", a prominent peak at 32.8 kHz and a smaller one at 12.3 kHz (Fig. 5). The observed frequency peak at 32.8 kHz correlates to the main resonance of the PZT ceramic element of the sensor and was observed for all HAE sensors of type *GMuG-Ma-Blc-30-35*. The origin of the secondary resonance peak at 12.3 kHz for the HAE sensors

is unknown. It is not a resonance resulting from attaching the HAE sensors to hydraulic tubing because it is seen for all the different HAE sensor installations. However, it is not seen on the HAE sensor prototype. More data especially for HAE sensors attached to hydraulic tubing are required for further more detailed analysis.

Due to the different orientations and lengths of the down-dipping boreholes equipped with HAE sensors, as well as documented water level fluctuations in the borehole between the surveys, we would not expect tube waves to exhibit the same stable frequency peak (e.g. 12.3 kHz) for all the different surveys.

We do not see that coupling depends on the down-dipping angle of the borehole due to the normal force resulting from the weight of the sensor on the sensor-borehole wall interface. As all boreholes were fully cored, we find the borehole wall to be smooth at the locations of the HAE sensors, because prominent structures were identified e.g. by televiewer logs, (c.f., Fig. 2 of Boese et al. 2022) and avoided. We conclude that a smooth borehole wall seems to provide sufficient sensor-rock coupling when the sensor is in contact with it.

We do not see changes in resonances due to HAE re-installation (e.g. panel for H17H of Fig. 5). We do see changing noise conditions between different field campaigns, that affect both AE and HAE sensors (e.g. during survey 0312) and are likely due to other activities in the mine.

4.3 Phase Characteristics

Given the complex character of the recorded wavefield in water-filled boreholes due to acoustic modes known as "tube-waves", S-waves are difficult to identify for HAE sensors. This is due to tube waves having one to two orders-of-magnitude higher amplitudes than any seismic body wave of interest in crystalline rocks (Cheng and Töksoz 1982). From an observational point of view, we consider S-waves difficult to identify on HAE traces, because of a complex coda after the first arriving wave with few distinct secondary arrivals, possibly due to S-wave getting converted to pressure waves at the water–rock interface.

Polarity picking is possible for P-wave arrivals recorded by the HAE sensors, as onsets are emergent but of high frequency. However, polarities are considered more uncertain overall compared to those polarities obtained for AE sensors, which are visibly more impulsive and of lower frequency content. We suspect that high frequencies of UT signals are damped due to the large distances between UT source and AE sensors compared to distances to HAE sensors. The location residual distribution (Supplementary Information Fig. S5) is comparable despite HAE sensors having more emergent, higher-frequency onsets versus AE sensors having more impulsive, low-frequency onsets.

We observed a systematic polarity reversal of the HAE sensors compared to the side-view AE sensors for active UT measurements with clearly defined polarity. We could exclude that the polarity reversal was caused by the recording system. We reproduced our in-situ observations in a simplistic calibration test using the impact of a salt grain on the sensor to test the polarity. Dropping the salt grain onto the face of the HAE sensor (axial direction) resulted in the same polarity as observed for a side-view AE sensor. However, when the salt grain was dropped onto the side of the HAE sensor (radial direction), it resulted in the inverse polarity as observed in the field. Because waves in the field reached the HAE sensors dominantly from the side, the salt grain test confirmed that it is not the installation technique that introduces a polarity reversal, but it is the sensors internal construction that defines the polarity.

The field observations from all the UT measurements suggest that the first arriving waves travel through the rock mass with incidence from the side at the HAE sensor through the contact with the borehole wall (therefore causing a reversal of the polarity and resulting in larger amplitudes than recorded by HAE sensors on hydraulic tubing surrounded by the water). HAE sensors were often installed at half-depth or total depth of the down-dipping boreholes. Waves travelling in the water column arriving in axial direction are recorded as later arrivals. Frontal incidences at the HAE sensor are unlikely for most of the sensor positions given the geometry of the boreholes, because of the predominantly shallow to intermediate-dipping boreholes hosting the HAE sensors (Fig. S2 of the Supplementary Information). We have a few ray geometries where wave incidence angles at the hydrophone-like sensors are $< 25°$, and these may have the same polarity rather then reversed compared to side-view AE sensors. However, our observations are too few and too emergent to systematically analyse polarity for incidence in the axial direction of the HAE sensors.

4.4 Advantages and Disadvantages of HAE Sensors in Adaptive Network Layouts

Pairing of the HAE sensors with hydraulic equipment worked well because the noise caused by fluid injection at the decametre scale is of different frequency content than the recorded AE signals (Fig. 4). This offers a simple yet effective means to improve the network geometry, detection and location capabilities of induced events in decametre scale experiments without requiring extra monitoring boreholes. By changing the positions of the HAE sensors for each stimulation interval we addressed any AE event detection issues arising from the stationary monitoring network during the STIMTEC experiment. We decided for repositioning HAE sensors for each stimulation interval

given the limited number of monitoring sensors available. However, repeated shifting of sensors caused a considerable operating workload and enormous data processing effort. Sensor positions had to be meticulously documented onsite, adding to the uncertainty in the data processing.

Using an adaptive seismic monitoring network improved locations of induced AE events. For the example intervals 28.1 and 30.2 m in the centre of the stationary and the adaptive monitoring networks discussed here, the reduction in the azimuthal gap is 13°. The location uncertainty achieved by using the HAE sensors close to the stimulated interval is approximately half of that obtained with the stationary network without HAE sensors, especially in the vertical direction (Table 1). This is due to an improved 3-D sensor coverage. However, using HAE sensors resulted in significantly lower numbers of identified S-wave arrivals (Table 1), which is difficult to properly account for in the location comparison between the two example intervals as S-arrivals can significantly influence the location accuracy. Our approach is to first obtain a location from P-wave arrivals only and then to add only S-wave arrivals consistent with this location (Boese et al. 2022). This should render the location comparison of the AE events from the two stimulation intervals unaffected by the actual number of S-wave arrivals used for the location process. Nevertheless, it stresses the fact that a monitoring network comprising only HAE sensors is not ideal, as it would result in too few and uncertain S-arrivals which are important for constraining the location. Therefore, we recommend a hybrid setup that allows us to make the best use of the existing borehole inventory. If HAE sensors cannot be placed close (< 17 m) to stimulated intervals, they should either be cemented in place or pneumatically coupled AE sensors should be used.

5 Summary and Conclusions

In the framework of the STIMTEC and STIMTEC-X hydraulic stimulation experiments, we tested an experimental way to install AE sensors without optimal coupling (cementing) in open, water-filled boreholes (HAE sensors). To assess performance measures such as frequency bandwidth, sensitivity, coupling and placement quality as well as the polarity of the HAE sensor, we performed a series of active UT measurements from boreholes with different orientations. We observe that the HAE sensors do not require optimal coupling (cementing) if placed close enough (within a 17 m distance) to the sources of the seismic signals. If attached to hydraulic tubing, so that pressure waves are recorded, we observe a factor 5.3 lower amplitudes compare to side-view AE sensors. Nevertheless, we consider the use of the HAE sensors beneficial, even without proper coupling to the rock mass. The HAE sensors record the wavefield adequately for first-arrival identification, polarity picking and amplitude characteristics of first arrivals. Furthermore, the amplitude sensitivity of the HAE sensor is less distorted for angles in the opposite direction in which the sensor is facing than side-view AE sensors, due to the internal design of the two different sensor types. HAE sensors are less suitable for detecting S-waves, thus a hybrid network of movable HAE and fixed AE sensors is recommended. The relative ease of installation of the HAE sensor in combination with hydraulic equipment allows us to effectively use the existing borehole inventory for hydraulic and seismic measurements simultaneously. Pairing of HAE sensors with the double packer probe represents a major network performance upgrade, as this allows for significantly improve AE event detection rate and quality of AE hypocentre locations during decametre scale hydraulic stimulations with experiment geometries like in STIMTEC. Flexibility in the installation of HAE sensors allows to optimize of the seismic network coverage. Consequently, azimuthal gaps are reduced and a more even polarity distribution on the focal sphere of focal mechanism solutions leads to smaller uncertainties in focal mechanisms.

Supplementary Information The online version contains supplementary material available at https://doi.org/10.1007/s00603-023-03418-9.

Acknowledgements This research has been supported by the Bundesministerium für Bildung und Forschung (grants no. 03G0874C and 03G0901C). We thank LfLUG for providing a mine layout of the Reiche Zeche mine complex. Logistic support by Frank Reuter and his team of miners at Reiche Zeche is gratefully acknowledged. We thank Christopher Wollin for help with visualising waveforms in Matlab. We very much appreciate the insightful comments by the reviewers and their helpful suggestions that improved this analysis.

Author contributions CMB, TF, GK and GD: planned the application of hydrophone-like AE-sensors during the experiments; CMB, TF, KP and GK: conducted fieldwork, CMB: administered the project, performed data curation with the help of TF, formally analysed the data and led the investigations. KP: performed polarity calibration tests in the lab and advised on data interpretation. CMB: wrote the manuscript with feedback and reviews by KP, GD, and GK. GD: acquired financial support for this project.

Funding Open Access funding enabled and organized by Projekt DEAL.

Data availability The ultrasonic transmission data are available here: https://doi.org/10.5880/GFZ.4.2.2021.002 and (the latter doi has the following temporary link until acceptance of the publication: https://dataservices.gfz-potsdam.de/panmetaworks/review/ba8625e0b484ca37eabf7477261f3279d45c0e9934a536fc79d9a6b13718464a/).

Declarations

Conflict of interest KP and TF are members of the company that manufactures the sensors used in this study.

References

Adero B (2020) Experimental investigations of mechanical anisotropy of Freiberg gneiss: implications for hydraulic stimulation, Ph.D. thesis, Ruhr-Universität Bochum

Blanke A, Boese C, Dresen G, Bohnhoff M, Kwiatek G (2023) Meter-scale damage zone characterization using s-coda waves from active ultrasonic transmission measurements in the STIMTEC project, URL Reiche Zeche, Germany. Geophys J Int. https://doi.org/10.1093/gji/ggad003

Boese CM, Kwiatek G, Fischer T, Plenkers K, Starke J, Blümle F, Dresen G, Janssen C (2021) Ultrasonic transmission measurements from six boreholes from the STIMTEC experiment, Reiche Zeche Mine, Freiberg (Saxony, Germany). GFZ Data Services. https://doi.org/10.5880/GFZ.4.2.2021.002

Boese CM, Kwiatek G, Fischer T, Plenkers K, Starke J, Blümle F, Janssen C, Dresen G (2022) Seismic monitoring of the STIMTEC hydraulic stimulation experiment in anisotropic metamorphic gneiss. Solid Earth Discuss. https://doi.org/10.5194/se-2021-84

Cheng CH, Töksoz MN (1982) Generation, propagation and analysis of tube waves in a borehole. SPWLA 23rd Annual Logging Symposium, January 1982. Society of Petrophysicists and Well-Log Analysts

Eisenblätter J, Spies T (2000) Ein Magnitudenmaß für Schallemission und Mikroakustik, 12. Kolloquium Schallemission, Jena, Berichtsband 72 der DGZfP, pp 29–41

Gibowicz S, Young R, Talebi S, Rawlence D (1991) Source parameters of seismic events at the underground research laboratory in Manitoba, Canada: Scaling relations for events with moment magnitude smaller than- 2. Bull Seismol Soc Am 81:1157–1182

Ikeda R, Tsukahara H (1983) Acoustic emissions detected by hydrophones during hydraulic fracturing stress measurements. Proc. hydraulic fracturing stress measurements workshop. National Academy Press, Washington, DC, pp 210–214

Jiménez Martínez VA (2021) Hydraulic changes induced by stimulation, Ph.D. thesis, Ruhr-Universität Bochum. https://doi.org/10.13154/294-7815

Kwiatek G, Plenkers K, Dresen G (2011) Source parameters of picoseismicity recorded at Mponeng deep gold mine, south Africa: implications for scaling relations. Bull Seismol Soc Am 101:2592–2608

Manthei G, Eisenblätter J, Spies T, Eilers G (2001) Source parameters of acoustic emission events in salt rock. J Acoust Emiss 19:100–108

Moriya H, Naoi M, Nakatani M, van Aswegen G, Murakami O, Kgarume T, Ward AK, Durrheim RJ, Philipp J, Yabe Y, Kawakata H, Ogasawara H (2015) Delineation of large localized damage structures forming ahead of an active mining front by using advanced acoustic emission mapping techniques. Int J Rock Mech Min Sci 79:157–165. https://doi.org/10.1016/j.ijrmms.2015.08.018

Naoi M, Nakatani M, Horiuchi S et al (2014) Frequency-magnitude distribution of $-3.7 \leq M\ W \leq 1$ mining-Induced earthquakes around a mining front and b value invariance with post-blast time. Pure Appl Geophys 171:2665–2684. https://doi.org/10.1007/s00024-013-0721-7

Naoi M, Nakatani M, Kgarume T, Khambule S, Masakale T, Ribeiro L, Philipp J, Horiuchi S, Otsuki K, Miyakawa K, Watanabe A, Moriya H, Murakami O, Yabe Y, Kawakata H, Yoshimitsu N, Ward A, Durrheim R, Ogasawara H (2015a) Quasi-static slip patch growth to 20 m on a geological fault inferred from acoustic emissions in a South African gold mine. J Geophys Res Solid Earth 120:1692–1707. https://doi.org/10.1002/2014JB011165

Naoi M et al (2015b) Unexpectedly frequent occurrence of very small repeating earthquakes ($-5.1 \leq M\ W \leq -3.6$) in a South African gold mine: implications for monitoring intraplate faults. J Geophys Res Solid Earth 120:8478–8493. https://doi.org/10.1002/2015JB012447

Ohtsu M, Aggelis DG (2022) Sensors and instruments. Acoustic emission testing. Springer, Cham, pp 21–44 (**ISBN ISBN 978-3-030-67936-1**)

Phillips WS (2000) Precise microearthquake locations and fluid flow in the geothermal reservoir at Soultz-sous-Forets, France. Bull Seismol Soc Am 90:212–228

Plenkers K, Manthei G, Kwiatek G (2022) Underground in-situ acoustic emission in study of rock stability and earthquake physics. Acoustic emission testing. Springer, Cham, pp 403–476

Plenkers K, Reinicke A, Obermann A, Gholizadeh Doonechaly N, Krietsch H, Fechner T, Hertrich M, Kontar K, Maurer H, Philipp J, et al (2023) Multi-disciplinary monitoring networks for mesoscale underground experiments: advances in the bedretto reservoir project. Sensors 23(6):3315. https://doi.org/10.3390/s23063315

Plenkers K, Kwiatek G, Nakatani M, Dresen G (2010) JAGUARS Research Group: Observation of seismic events with frequencies $f > 25$ kHz at Mponeng Deep Gold Mine, South Africa. Seismol Res Lett 81:467–479. https://doi.org/10.1785/gssrl.81.3.467

Renner J (2021) STIMTEC-Team: STIMTEC – A mine-scale hydraulic stimulation experiment of anisotropic metamorphic rock with evaluation by mine-back drilling. In: Ma X (ed) Introduction to the special issue: deep underground laboratories (DUL), ARMA Newsletter Winter 2021, 2–4, ARMA Publications Committee. https://www.armarocks.org/wp-content/uploads/2021/01/2021_issue_30_winter.pdf (last access: July 2023)

Schoenball M, Ajo-Franklin JB, Blankenship D, Chai C, Chakravarty A, Dobson P, Hopp C, Kneafsey T, Knox HA, Maceira M, Robertson MC, Sprinkle P, Strickland C, Templeton D, Schwering PC, Ulrich C, Wood T, EGS Collab Team (2020) Creation of a mixed-mode fracture network at mesoscale through hydraulic fracturing and shear stimulation. J Geophys Res Solid Earth. 125:e2020JB019807. https://doi.org/10.1029/2020JB019807

Stein S, Wysession M (2003) An introduction to seismology. Earthq Earth 7(9):10

Vervoort A, Min K-B, Konietzky H, Cho J-W, Debecker B, Dinh Q-D, Frühwirt T, Tavallali A (2014) Failure of transversely isotropic rock under Brazilian test conditions. Int J Rock Mech Min Sci 70:343–352. https://doi.org/10.1016/j.ijrmms.2014.04.006

Villiger L, Gischig VS, Doetsch J, Krietsch H, Dutler NO, Jalali M, Valley B, Selvadurai PA, Mignan A, Plenkers K, Giardini D, Amann F, Wiemer S (2020) Influence of reservoir geology on seismic response during decameter-scale hydraulic stimulations in crystalline rock. Solid Earth 11:627–655. https://doi.org/10.5194/se-11-627-2020

White JE (1953) Signals in a borehole due to plane waves in the solid. J Acoust Soc Am 25:906–915

Wollin C, Bohnhoff M, Martínez-Garzón P, Küperkoch L, Raub C (2018) A unified earthquake catalogue for the Sea of Marmara Region, Turkey, based on automatized phase picking and travel-time inversion: Seismotectonic implications. Tectonophysics 747:416–444